Guefoams (guest-containing foams) as novel heterogeneous catalysts: Preparation, characterization and proof-of-concept testing for CO_2 methanation

L.P. Maiorano, C.Y. Chaparro-Garnica, E. Bailón García, D. Lozano-Castelló, A. Bueno-López, J.M. Molina-Jordá [*]

Department of Inorganic Chemistry, University of Alicante, Carretera de San Vicente del Raspeig s/n, E03080 Alicant, Spain

HIGHLIGHTS

- The replication approach was used to prepare a Guefoam of Al-12Si alloy matrix containing $Ni/CeO_2/Al_2O_3$ particles as guest phases.
- The as-prepared Guefoam has poor catalytic activity due to chlorine poisoning of the active phase, which significantly increases after calcination.
- Guefoam offers up to 170% higher permeability and up to 146% higher catalytic performance in CO_2 methanation than particle bed.
- The high thermal conductivity of the Guefoam (43 $Wm^{-1}{}^{\circ}C^{-1}$) enables the design of large reactors with minimum radial temperature gradients.

GRAPHICAL ABSTRACT
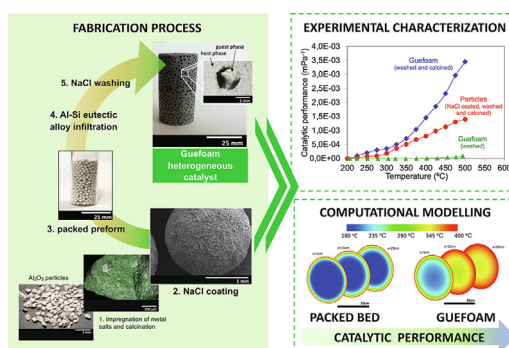
ABSTRACT

The preparation and use of Guefoams as heterogeneous catalyst is reported. The Guefoam catalyst consists of an open-pore Al-Si foam that accommodates a freely mobile guest phase ($Ni/CeO_2/Al_2O_3$ particles) in its cavities, with neither a physical nor a chemical matrix-guest bond. A eutectic Al-12Si alloy was used as a low-melting matrix precursor to prevent thermal sintering of the active phase during liquid metal infiltration. CO_2 methanation was chosen as the reaction test. The activity and CH_4 selectivity (close to 100%) achieved with the Guefoam catalyst were similar to those obtained with a packed bed of the same active phase particles, but with the advantages of a structured reactor such as robustness and ease of handling. The thermal conductivity of the Guefoam catalyst is significantly improved with regard to the packed bed of active phase particles, which reduces the temperature gradients in the catalytic reactor, as demonstrated by computational fluid dynamic modelling. Since the permeability of the Guefoam catalyst is 2.7 times that of the packed bed, the pressure drop caused by the passage of a fluid through the novel material is reduced, resulting in a significantly higher catalytic performance index than the packed bed.

© 2022 The Authors. Published by Elsevier Ltd. This is an open access article under the CC BY-NC-ND license (http://creativecommons.org/licenses/by-nc-nd/4.0/).

---

* Corresponding author.
  E-mail address: jmmj@ua.es (J.M. Molina-Jordá).

1. Introduction

The so-called Guefoams (guest-containing foams) are a new family of recently developed materials that are attracting increasing attention due to their promising behaviour in several applications. Guefoams consist of multifunctional porous materials hosting granular or fibrous phases with specific functionality (guests) in open-pore foam (host) cavities [1–4]. There is no bonding between the host matrix phase (the phase that forms the porous skeleton) and the guest phases other than mere physical contact. For this reason, the entire surface of the guest phases is functional, and a fluid can flow through the Guefoam with a relatively low pressure drop. Guefoams were conceived to provide broader or newer functionalities to conventional foams or those incorporating new phases by full or partial embedding in the matrix phase. The Guefoams manufacturing process is simple and economically feasible for large-scale production, as it is based on the conventional replication method commonly used to produce most foams on the market today. The production consists of infiltrating a foam matrix precursor under gas pressure into pre-forms containing guest phases in the form of particles or fibres coated with NaCl, which is dissolved after solidification of the matrix precursor [5,6]. As an example, Guefoams with an aluminium matrix phase containing both steel and activated carbon particles as guest phases have been reported for the preconcentration and desorption of volatile organic compounds (VOCs) by rapid magnetic induction heating [3]. Recently, magneto-inductive carbon matrix Guefoams with embedded iron nanoparticles and activated carbon as guest phase have been shown to be effective VOC preconcentrators [4].

Conventional foams are used as catalyst supports, whose intricate interconnected porous structure enables the development of a higher specific surface area per unit volume than honeycomb monoliths. The interaction of fluids with active phases loaded on foams is generally greater than in honeycombs, since fluids usually adopt laminar flow in honeycomb channels, while foams favour a turbulent regime, which improves mass and heat transfer [7]. In addition, foams also undergo a moderate pressure drop, which can be tailored by controlling the size of the interconnection windows between pores.

However, given the complex pore space of foams, loading of active catalytic phases is often non-trivial for these materials [8]. Some examples of loading foams with active phases have been described by electrochemical or hydrothermal processes for Ru-Ce/Ni [8], Ni-SiO$_2$/GO-Ni [9], BiFeO$_3$/Ni [10], Cu(NP)s/Gf-Ni [11], Co-W-B/Ni [12], Ni/SiC [13], ZSM-5/SiC [14] and MOF/SiC [15]. Recently, open-pore graphite foams derived from mesophase pitch have been developed in which TiC nanoparticles are conveniently distributed in two positions (on the pore surface and in the foam struts) [16]. Depending on their location, the TiC nanoparticles fulfil two different roles: those at the struts catalyse the pitch graphitization process and allow high thermal conductivity to be achieved, while those anchored on the pore surface can serve as metal supports for catalytic purposes. These particles at the pore surface are partially embedded in the matrix phase. A major drawback of the embedded phases is that they lose part of their surface area, which significantly reduces their surface functionality.

Despite the interesting features of foams as catalyst supports, the use of Guefoams in heterogeneous catalysis has not been developed yet. These materials have great design potential, which makes them even more interesting than conventional foams as catalytic supports. Its processing, besides being simple and economically feasible for large-scale production, avoids the difficult step of active phase loading. In addition, Guefoams can be prepared with a

metal matrix and their high thermal conductivity promotes heat transfer from or into the catalyst phases. This contributes to the catalytic conversion rate of a reactor having a more homogeneous radial distribution than that of a particle bed, allowing larger reactors to be built with higher catalytic efficiency. Moreover, Guefoams have the advantage of being materials that can be customized by varying design parameters such as the fraction of pores occupied by the guest phase(s) or the volume fraction that they occupy in the porous cavity, which allows modification of properties that are important for fluid dynamic applications, such as permeability or relative pressure drop [3,4]. This design versatility enables the development of catalytic reactors with higher efficiency and consequently lowers operating costs, in line with near-term expectations for heterogeneous catalysis in the context of greener and more energy-efficient chemical processes. Guefoams have such high design potential for catalytic purposes that they can successfully meet challenges that numerous scientists have proposed as research topics in the field of heterogeneous catalysis for the coming years. By using Guefoams, scientists could make scientific progress in designing reactors for multi-catalysis or simultaneous tandem catalysis by combining guest phases with different catalytic functions and differentiated localization [17,18].

The preparation and applicability of Guefoams as heterogeneous catalysts were investigated in this study. Alumina particles loaded with a Ni/CeO$_2$ active phase were used as a guest phase hosted in a Al-Si foam. The resulting material was tested for methane production by CO$_2$ hydrogenation. This reaction is of practical relevance to reduce CO$_2$ emissions to the atmosphere and to produce a valuable fuel that can be easily distributed through the existing natural gas network [8,9,19–25]. This reaction will become particularly important in a new energy scenario, where H$_2$ will be massively obtained from renewable energy sources, as CO$_2$ methanation will be a chemical route for energy storage. The selected active phase is one of the most efficient noble metal-free CO$_2$ methanation catalysts of practical interest [26]. The aim of this study is therefore not to investigate the methanation reaction or the active phase behaviour, as this has already been studied by several researchers [20,27–29], but to use this reaction and the active phase as a proof of concept to evaluate the potential applicability of the novel Guefoam catalyst. A multidisciplinary team with metallurgical and catalytic background was necessary to optimize the manufacturing process and avoid thermal and chemical degradation of the active phase.

2. Experimental procedures

2.1. Preparation of catalyst particles

A Ni/CeO$_2$/Al$_2$O$_3$ active phase was prepared with the following nominal composition: 5 wt% Ni + 47.5 wt% CeO$_2$ + 47.5 wt% Al$_2$O$_3$. The composition was confirmed by ICP-AES. Commercial α-Al$_2$O$_3$ pellets were ground and sieved to produce Al$_2$O$_3$ particles of 0.75–1 mm, which were first impregnated with cerium (III) nitrate hexahydrate. After calcination at 500 °C for 2 h (heating at 5 °Cmin^{-1}), nickel (II) nitrate hexahydrate was further impregnated, dried and calcined at 450 °C for 2 h (heating at 5 °Cmin^{-1}). The above three raw materials were supplied by Alfa-Aesar (Kandel, Germany).

2.2. Fabrication of Guefoam materials

The catalyst particles were coated with NaCl (99.5 wt%; Panreac Química S.L.U., Barcelona, Spain) by spray coating with a 20 wt% NaCl-water solution, as described elsewhere [1–4]. The coated par-

L.P. Maiorano, C.Y. Chaparro-Garnica, E. Bailón García et al.

Materials & Design 217 (2022) 110619

ticles were sieved and fractions with a diameter of 1.7–2.2 mm were used for the Guefoam catalyst preparation.

Replication method was followed to prepare the Guefoam catalyst [30,31]. The coated guest phase particles were packed with the help of vibrations into a graphite crucible with an inner diameter of 26 mm and a height of 100 mm, which had been previously sprayed with a BN coating (ZYP Coatings Inc., Oak Ridge, USA) to facilitate demoulding (see more details in [32] for the packing procedure). To prevent the particles from moving or floating during metal infiltration, a 2 mm thick graphite disk with holes of about 0.5 mm was properly fixed to the top of the compacted preform. A eutectic aluminium–silicon alloy (Al-12 wt% Si), prepared with commercially pure aluminium (99.95 wt%) and silicon powder (99.9 wt%) both purchased from Alfa Aesar (GmbH & Co KG-Karlsruhe, Germany), was used as the metal matrix precursor. A solid piece of aluminium alloy was placed on top of the graphite disk and the crucible was then inserted into a gas pressure infiltration chamber [33,34]. A vacuum up to 0.2 mbar was applied, with a heating rate of 4.5 °Cmin^{-1} up to 665 °C. After 10 min at constant temperature, the vacuum was closed and the chamber was pressurized with 0.8 bar argon to infiltrate the packed preform with liquid metal.

After infiltration, the chamber was rapidly cooled at 50 °Cmin^{-1} to solidify the metal. The solid was extracted by removing the surrounding excess metal. This yielded a piece 25 mm in diameter and 45 mm in length containing 350 mg of active phase particles. The sodium chloride coating was removed by dissolution with a pressurized water flow, as described in [35]. The result was an interconnected Al-Si alloy pore structure in which the guest phase particles are located inside the porous cavities without chemical or physical bonding. The Guefoam catalyst was finally calcined at 500 °C for 4 h, and catalytic tests were performed with the Guefoam catalyst before and after this heat treatment.

2.3. Micro-, macro- structural characterization

The guest phase particles and the surface morphology of their NaCl coating were characterized using a SEM-Hitachi S3000N scanning electron microscope operating at variable voltage. The spatial distribution of the Ni active phase and the composition of the guest phase particles were analysed using the same microscope equipped with a Bruker XFlash 3001 X-ray detector for point and map analysis (EDX).

Geometric parameters (circularity and aspect ratio) were determined from image analysis. Circularity is defined as $4 \cdot \pi \cdot area/perimeter^2$, where 1.0 represents perfect circularity. The aspect ratio is the ratio between the average major and minor axes of the particles. These last two parameters were determined from measurements of over 300 particles.

The density of the active phase particles was measured by densitometry using dichloromethane (density = 1.330 gcm^{-3} at 25 °C) according to the ASTMD854 standard. The use of dichloromethane avoids the dissolution of the NaCl used as coating of the active phase particles.

2.4. Thermal conductivity measurement

Thermal conductivity was experimentally determined by a set-up assembled at the University of Alicante laboratories in compliance with the international standard ASTM E-1225-04, based on a relative steady-state (equal-flow) technique [35–37]. Each sample, with cylindrical geometry, was placed between two blocks. The bottom of the sample remained in contact with a cooled cylindrical block (refrigerated by a room temperature water flow) and the top was in contact with a brass reference block connected to a 70 °C water bath. Two sets of thermocouples were connected to the sample and three more to the brass reference so that the temperature gradients required to estimate thermal conductivity could be measured with an uncertainty of less than ±5%.

2.5. Characterization by X-ray photoelectron spectroscopy (XPS)

XPS characterization was performed in a K-ALPHA Thermo Scientific device using Al-Kα radiation (1486.6 eV) and a twin crystal monochromator that yields a focused X-ray spot with a diameter of 400 μm at 3 mA × 12 kV. The binding energy scale was adjusted by setting the C1s transition to 284.6 eV.

2.6. Catalytic tests

CO_2 methanation experiments were carried out in a cylindrical reactor with a 64% H_2 + 16% CO_2 gas mixture balanced with N_2 (100 mlmin^{-1} total flow and atmospheric pressure). The experiments were performed with a packed bed of the active phase particles between quartz wood plugs and with the Guefoam catalyst. In both cases, the amount of catalyst particles was 350 mg. Gas composition was monitored using specific AwiteFLEX COOL gas analysers, with NDIR, electrochemical and TCD detectors for CO, CO_2, CH_4, O_2 and H_2. The catalysts were pretreated with 50% H_2/N_2 at 500 °C for 1 h and cooled to room temperature under inert gas. Then the reaction mixture was fed into the reactor and the gas composition was measured under steady-state conditions at selected temperatures from room temperature to 500 °C.

2.7. Pressure drop measurements

The gas flow pressure drops generated by the novel Guefoam catalyst and a packed bed of active phase particles were determined experimentally using the setup described in Fig. 1.

The permeability (k) can be derived from the Darcy-Forchheimer equation, which relates the fluid velocity (v) and the pressure drop ($\Delta P/\Delta L$). This equation contains the viscous term of Darcy's law and the inertial effects generated by the flow in the porous medium [5,37]:

$$\frac{\Delta P}{\Delta L} = \frac{\mu}{k} v + \rho C_i v^2 \tag{1}$$

where μ and ρ are the dynamic viscosity and density of the fluid (taken as 1.85×10^{-5} kgm^{-1}s^{-1} and 1.184 kgm^{-3} at 25 °C, respectively). C_i refers to the inertial coefficient. The viscous loss (v·μ/k) is linear with velocity and includes a viscous resistance coefficient of 1/k, which is the inverse permeability. The inertia term ($\rho C_i v^2$) accounts for the nonlinear pressure behaviour as a function of fluid flow by including an inertial resistance coefficient C_i.

2.8. Radial temperature gradients by finite elements modelling

Temperature gradients within the Guefoam and the packed bed allow understanding how quickly a radial section of the reactor approaches the minimum and maximum temperatures of catalytic conversion, which mainly depends on the permeability and thermal conductivity of the material as well as fluid velocity. Radial temperature gradient calculations were performed with the ANSYS Fluent software package using a computational fluid dynamic (CFD) approach. The software was employed to simulate the above materials using simplified porous media configuration under local thermal non-equilibrium (LTNE) conditions, which assumes the difference between fluid and solid temperatures in two energy equations. Real-dimensioned reactors of 30 cm length (L) and 15 cm diameter (d) with the composition and pore volume fraction of Guefoam and packed bed were modelled following the computational domain schematic diagram and boundary conditions
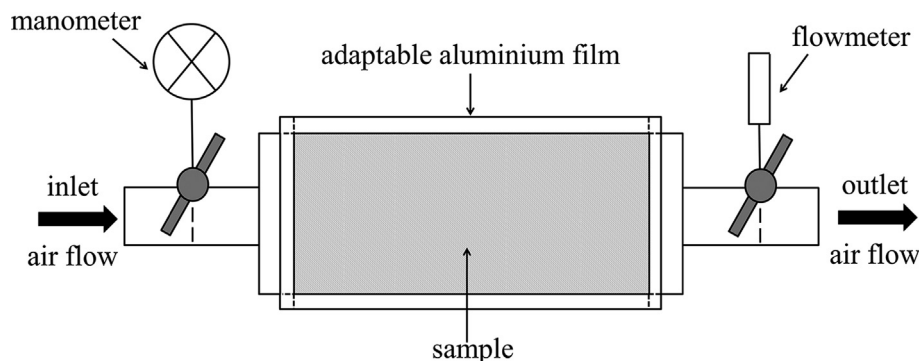
L.P. Maiorano, C.Y. Chaparro-Garnica, E. Bailón García et al.

Materials & Design 217 (2022) 110619

Fig. 1. Schematic diagram of the experimental setup used for the pressure drop measurements.

shown in Fig. 2. The system, considered to be at a constant temperature of 400 °C, was subjected to a fluid flow of 6×10^3 lmin^{-1}. The fluid was deemed incompressible with analogous air physical properties and inlet temperature of 180 °C. Heat losses due to convection or radiations were assumed to be negligible. The governing energy equations are as follows [38,39]:

Fluid energy equation:

$$\rho_f C_f v \cdot \nabla T_f = \varepsilon K_f \nabla^2 T_f + h_{sf} a_v (T_s - T_f) \qquad (2)$$

Solid energy equation:

$$(1 - \varepsilon) K_s \nabla^2 T_s + h_{sf} a_v (T_f - T_s) = 0 \qquad (3)$$

where ε is the pore volume fraction of the porous material, C is the specific heat, K is the thermal conductivity, T is the temperature, h_{sf} is the interfacial heat transfer coefficient and a_v is the interfacial area density. The subscripts f and s refer to the fluid and solid phases, respectively.

CO_2 methanation is an exothermic reaction that typically proceeds between 200 °C and 500 °C, depending on the catalyst and experimental conditions [19]. Its enthalpy is -165 KJmol^{-1} at 25 °C, but it decreases rapidly with temperature, becoming virtually nil at high temperatures close to its common operating limit [40]. In this context, it can be assumed that the heat released by the methanation reaction does not substantially alter the local temperature conditions of the catalytic monoliths, since the conversion rate at low temperatures is low and therefore the heat released can be considered negligible. At high temperatures, where the conversion rate is high, the heat released is also negligible due to the near zero enthalpy. Therefore, the effect of the heat released by the methanation reaction was not included in the modelling calculations of the temperature profiles.

3. Results and discussion

3.1. Characterization of active phase particles and NaCl-coated active phase particles

Fig. 3 shows several images of active phase particles before and after NaCl coating.

Fig. 3a and b show that the uncoated active phase particles have an angular geometry, whereas they become more spherical after coating with NaCl (Fig. 3c). This is confirmed by the circularity values listed in Table 1, which increase from 0.68 to 0.86 after NaCl coating, and by the aspect ratio values, which also increase from 0.68 to 0.89. Table 1 also compiles the densities determined by densitometry with dichloromethane.

Fig. 3b displays an EDX-Ni mapping on the surface of an active phase particle, which confirms the homogeneous spatial distribution of the active phase on the surface of the alumina particles. The thickness of the NaCl coating can be seen in Fig. 3d, which shows a profile after a controlled fracture. It should be noted that, since the active phase particles have an angular morphology, the thickness of the NaCl coating around each particle is not homogeneous. Using image analysis, the average diameters of both the uncoated and coated active phase particles were measured (see supplementary material for more information).
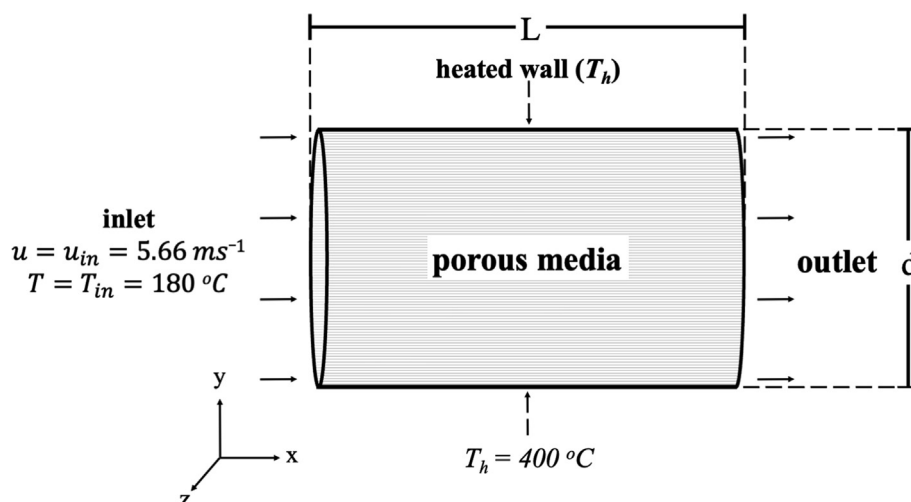

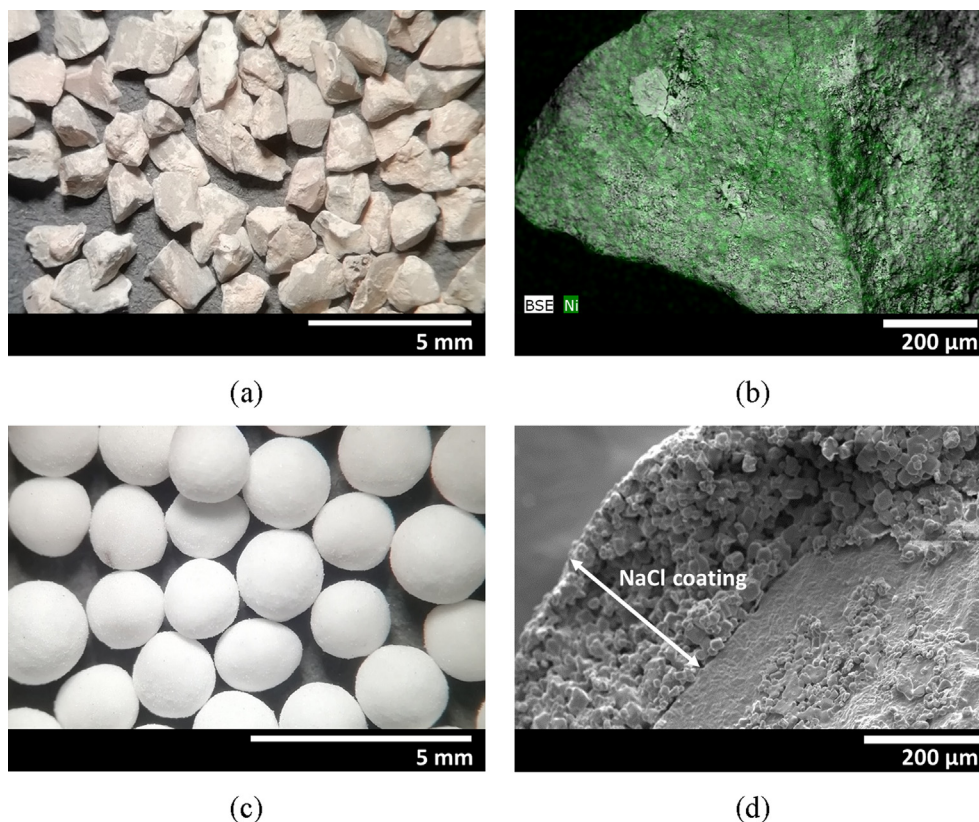**Fig. 2.** Schematic diagram and boundary conditions employed of the modelled, real dimensioned reactors.

L.P. Maiorano, C.Y. Chaparro-Garnica, E. Bailón García et al.

Materials & Design 217 (2022) 110619

Fig. 3. (a) Optical image of Al$_2$O$_3$ particles used to prepare the guest active phase, (b) SEM image of Ni/CeO$_2$/Al$_2$O$_3$ particles with EDX analysis of Ni in green, (c) optical image of sodium chloride coated active phase particles and (d) SEM image of a cross-section created by a deliberate fracture of the NaCl coating on an active phase particle.

Table 1
Densities of different materials determined by densitometry with dichloromethane and geometrical parameters (circularity and aspect ratio) determined by image analysis.

Material	Density (gcm^{-3})	Circularity	Aspect ratio
Active phase particles	3.148	0.68	0.68
NaCl-coated active phase particles	2.194	0.86	0.89
NaCl spheres (active phase-free NaCl spheres)	1.500	–	–

For the characterization of Guefoams, the guest loading (GL) and guest occupation (GO) parameters are essential:

$$GL = \frac{n_g}{N_p} \quad (4)$$

$$GO = \frac{v_g}{V_p} \quad (5)$$

where n$_g$ is the number of pores hosting a guest phase, N$_p$ is the total number of pores, v$_g$ is the average volume of guest phases and V$_p$ is the average volume of hosting pores.

GL represents the fraction of pores hosting a certain type of guest phase. This parameter is determined by the relative ratio between the amount of NaCl-coated active phase and the amount of massive NaCl spheres that do not contain active phase. In the present study, all the pores of the foam material were intended to host an active guest phase particle, i.e., the GL parameter should be as close as possible to 1 (or, as a percentage, 100%). The experimental results showed that the GL = 97% (supplementary material).

The GO parameter is the ratio between the average volumes of active phase particles and the cavities containing them. For fully spherical active phase particles and cavity geometries, GO=(r/R)^3, where r and R are the average radii of the uncoated active phase particles and NaCl-coated active phase particles, respectively. The calculation of the GO parameter in non-spherical geometries such as the current angular geometry of the active phase is not so straightforward. This parameter was determined in two independent ways and resulted in a percentage value of 42–43%, as explained in the supplementary material.

Although constant GO and GL values are employed in this work, given the proof-of-concept nature of the present research, both parameters can be modified to significantly alter the fluid dynamic behaviour of the fluid passing through the material. The effect of GO and GL on critical parameters such as permeability and relative pressure drop was demonstrated in [3].

3.2. Microstructural characterization of the Guefoam catalyst

The general structure of a Guefoam is depicted in Fig. 4a. Guefoams consist of an interconnected (or open-pore) foam material hosting freely moving guest phases in their cavities, since there is no chemical or physical matrix-guest bond. The dimensions and geometry of the Guefoam herein fabricated can be seen in the photograph in Fig. 4b. Fig. 4c provides an optical micrograph of the cavities containing the guest phases (Ni/CeO$_2$/Al$_2$O$_3$ active phase particles).

3.3. Catalytic tests

Experiments on CO$_2$ methanation were performed with a packed bed of active phase particles and with the Guefoam cata-
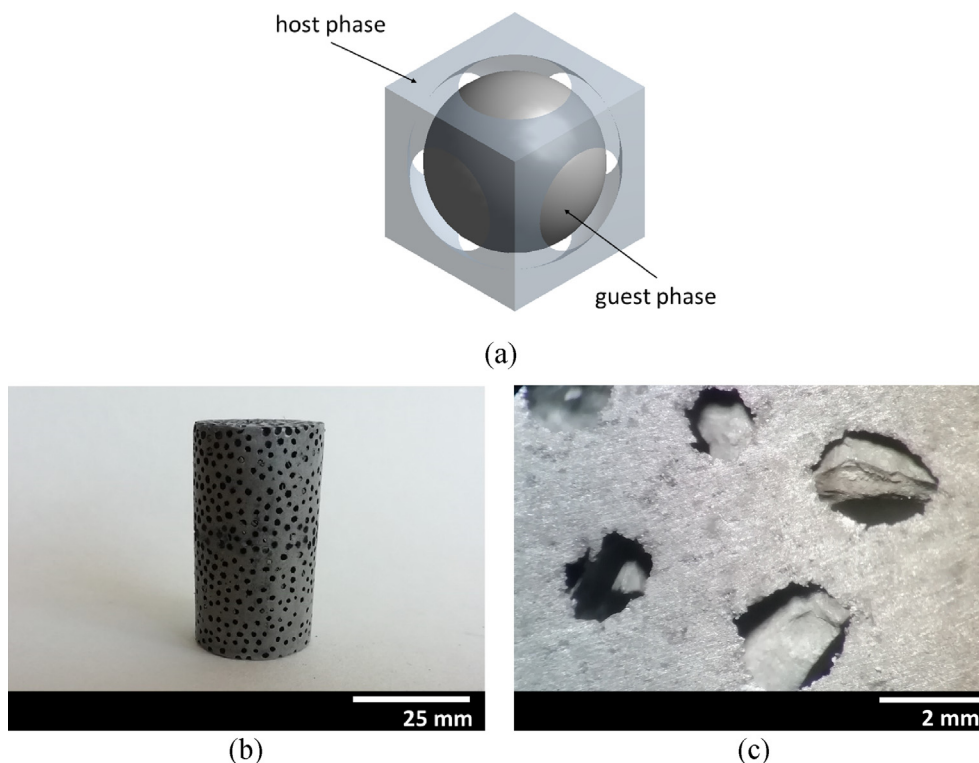
Fig. 4. (a) Schematic drawing of a unit cell representing a guest phase sphere (dark grey) in a cavity of the porous matrix (light grey); (b) photograph of the Guefoam and optical image (c) of a zoomed region in (b) showing some guest phase particles in porous cavities.

lyst. The results of CO_2 conversion and CH_4 selectivity are shown in Fig. 5.

The as-prepared Guefoam catalyst obtained after NaCl removal with water showed no activity (Fig. 5a; green triangles), and our hypothesis was that the active phase was poisoned by chlorine, consistent with what other authors have found about the inhibition of various active phases by chlorine species [43–45]. This hypothesis was confirmed by XPS characterization, and a detailed analysis is described in the next section. In order to reverse this chlorine poisoning, the monolith catalyst was calcined at 500 °C for 4 h, and then successful catalytic activity was achieved in CO_2 methanation. The onset reaction temperature was 225 °C, and thermodynamic equilibrium was reached at 500 °C. CH_4 selectivity was 100% up to 400 °C, and few CO was detected above this temperature, with selectivity dropping to 80% at 500 °C. This catalytic behaviour was compared with powder of Ni/CeO$_2$ active phases reported in the literature, as well as with our own previous catalytic results [26], and the onset CO_2 methanation temperature

obtained with the novel Guefoam catalyst prepared in this study is similar to that previously measured for Ni/CeO$_2$ powders. However, thermodynamic equilibrium was reached with Ni/CeO$_2$ powder at 350 °C, while this temperature was shifted to 500 °C in the current study. This indicates that the catalytic activity of the Guefoam catalyst is in some way lower than that of the active phase powder, and this is the penalty to be paid for the novel supported catalyst. Nevertheless, the catalytic activity of the novel monolith is high enough to be properly used.

A catalytic experiment was performed with the active phase particles subjected to the same treatments used for the preparation of the monolith catalyst (NaCl coating, washing and calcination) but without the AlSi foam support. The catalytic behaviour is similar for the particles and for the Guefoam catalyst, proving that the shape of the catalytic bed (particle or monolith) does not affect the catalytic behaviour under the experimental conditions of these tests. That is, the Guefoam catalyst is able to perform the same as the packed bed made of the same active phase particles, but
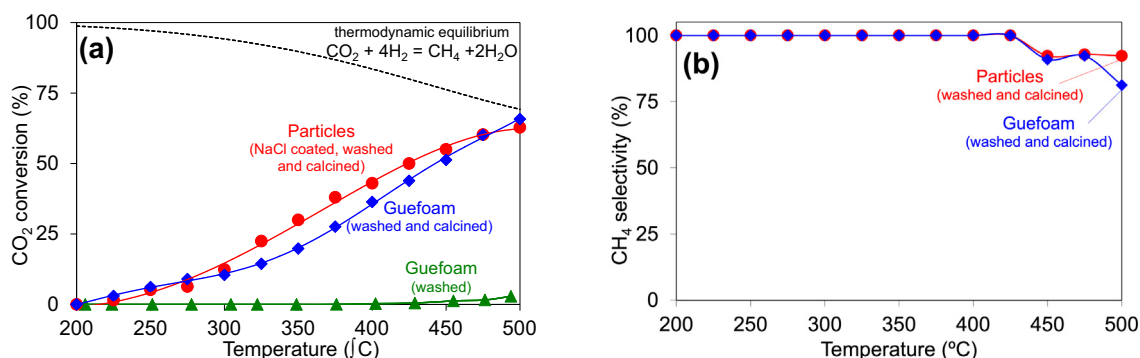

Fig. 5. CO_2 methanation catalytic tests: (a) CO_2 conversion and (b) CH_4 selectivity. Experiments were performed with a 64% H_2 + 16% CO_2 gas mixture balanced with N_2 at 100 mlmin^{-1} and atmospheric pressure. The calculations for thermodynamic equilibrium were performed according to the methodology and data published in [41,42].

L.P. Maiorano, C.Y. Chaparro-Garnica, E. Bailón García et al.

Materials & Design 217 (2022) 110619

with the benefits of a structured piece (easy manipulation, improved thermal conductivity due to the metal matrix, etc.).

3.4. XPS characterization

To analyse the effect of chlorine on the catalytic performance of the active phase, XPS analysis was performed on the active phase particles in the as-prepared state, after NaCl coating and washing, and after further calcination at 500 °C for 4 h. Fig. 6 shows the spectra obtained in different energy regions corresponding to Cl2p, Ni2p, Ce3d and O1s.

The presence of chlorine on the active phase was confirmed after NaCl coating and water washing (Fig. 6a), which is consistent with our hypothesis of chlorine poisoning. Calcination at 500 °C for 4 h removed part of the chlorine, and successfully activated the active phase, resulting in suitable catalytic activity.

In addition to the chlorine changes, additional changes were observed on the active phase surface after NaCl coating, washing and calcination. Fig. 6b shows the Ni2p region, and differences in the position of the main peak after the different treatments are distinguished. The detailed interpretation of Ni2p spectra is still a matter of debate, but information about the electronic environment of the nickel species can be obtained from the position of the main peak [46–49]. It has been reported that the main peak of metallic nickel appears at around 853 eV, while cationic species of Ni^{2+}, such as NiO or partially hydrated oxides, usually appear at 854 eV and higher energies. The values measured in our spectra confirm the presence of cationic nickel in all cases, but there is a shift in the position of the peak from 855.2 eV in the as-prepared particles to 855.9 eV after NaCl coating and washing. This 0.7 eV shift evidences a lower negative charge density on Ni^{2+} cations after NaCl coating and washing, consistent with a Ni^{2+}-Cl^- interaction. The Ni^{2+} main peak is further shifted to 856.4 eV after calcination treatment, indicating a significant change in the electronic environment of the nickel cations, which could be consistent with the partial substitution of chlorine by oxide anions.

The electronic density of the cerium cations (Fig. 6c) also changes before and after the different treatments. A mixture of Ce^{3+} and Ce^{4+} cations is usually found on ceria, and the Ce3d spectra combine the contributions of both types of cations, as shown in the graph. The percentage of Ce^{3+} cations slightly decreases from 21 % to 18 % after NaCl coating and washing. This oxidation is consistent with the chlorine-poisoning hypothesis and proves that chlorine affects not only nickel cations but also cerium cations. Stabilization of the oxidised state of cerium cations by the presence of chlorine probably inhibits the reversible Ce^{3+}/Ce^{4+} redox cycle required for proper catalytic activity. The percentage of Ce^{3+} cations increases significantly from 18% to 27% after calcination treatment. In accordance with the nickel behaviour, calcination treatment seems to replace chlorine by oxide also on ceria, allowing the partial reduction of Ce^{4+} to Ce^{3+}, which would explain the recovery of catalytic activity.

The increase in Ce^{3+} content upon calcination is consistent with the O1s spectra (Fig. 6d). The O1s spectra can be deconvoluted into different contributions. The peak at the lowest energy is attributed to lattice oxygen, while other peaks at higher energies are attributed to surface species such as carbonates, hydroxyl groups and chemisorbed oxygen on ceria vacancies associated with Ce^{3+} cations. The position of the oxygen lattice peak shifts from 428.7 eV to 429.3 eV after NaCl coating and washing, which may be a consequence of the presence of a highly electronegative element such as Cl. After thermal treatment, the position of this lattice oxygen peak shifts by 0.8 eV (from 429.3 eV to 530.1 eV), which is also consistent with the partial removal of chlorine. Special attention must be paid in this case to the surface oxygen species, whose contribution to the O1s spectra increases dramatically after calcination. This is consistent with the appearance of oxygen vacancies due to the increase in the proportion of Ce^{3+} cations during calcination, which are filled by chemisorbed oxygen.
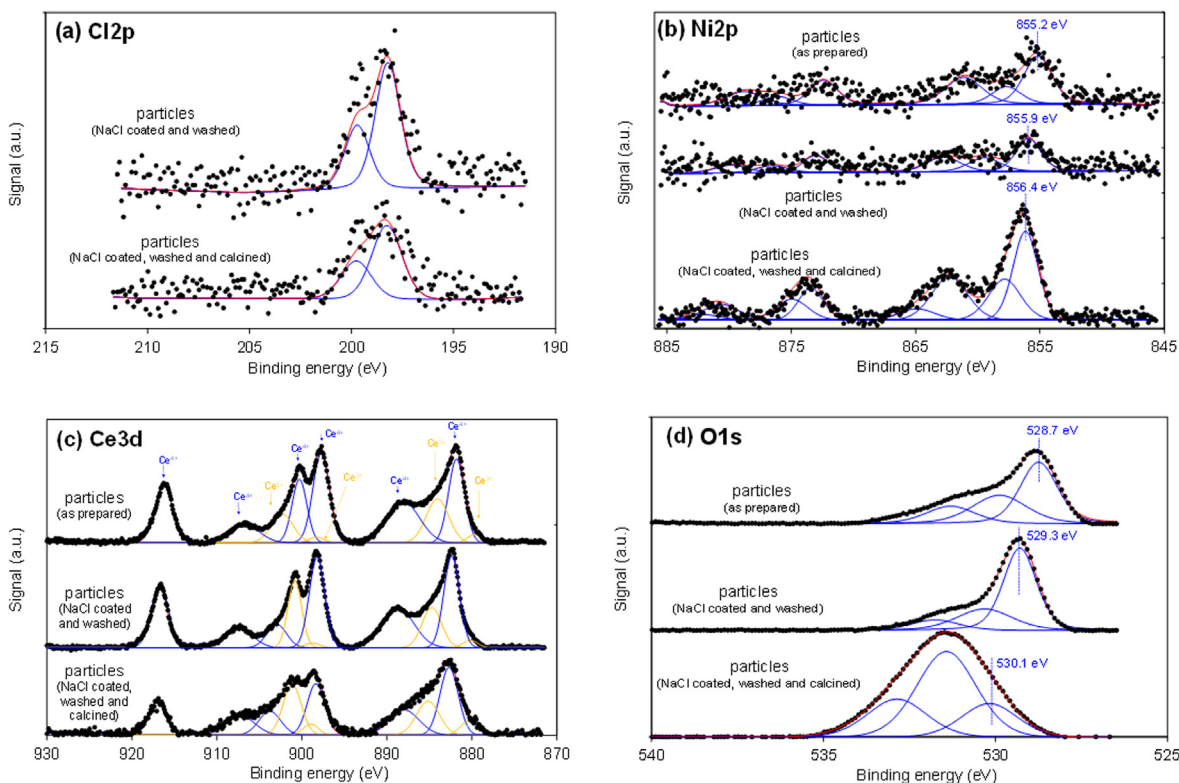

Fig. 6. XPS characterization of active phase particles in different energy regions. (a) Cl2p, (b) Ni2p, (c) Ce3d and (d) O1s.

L.P. Maiorano, C.Y. Chaparro-Garnica, E. Bailón García et al.

Materials & Design 217 (2022) 110619

In summary, XPS analysis confirms the presence of chlorine on the active phase after NaCl coating and washing, which is expected to inhibit the redox processes of the nickel and cerium cations required to achieve adequate catalytic activity. The negative effect of chlorine can be partially reversed by calcination at 500 °C for 4 h, and XPS analysis provides evidence for the substitution of chlorine by oxide with the expected restoration of redox behaviour.

3.5. Thermal conductivity

To further analyse the potential advantages of the novel Guefoam materials in catalytic applications, the thermal conductivity measurements are discussed in this section.

The measured thermal conductivities of the materials herein evaluated are summarized in Table 2. The thermal conductivity of the Guefoam catalyst is 43 $Wm^{-1}°C^{-1}$, which is significantly higher than that of the packed bed obtained by compacting the active phase particles, with a value of 1.7 $Wm^{-1}°C^{-1}$. The Guefoam value of 43 $Wm^{-1}°C^{-1}$ is consistent with the thermal conductivity measured for an analogous guest-free foam (i.e. GL = 0%). This confirms that the absence of chemical bonding between the matrix and the active phase is responsible for the nil contribution of the guest phases to the overall thermal conductivity of the material. Therefore, this conductivity value is consistent with the estimates that can be made with analytical models for metal foams [35–37], which state that.

$$K = K_s(1 - \varepsilon)^n \tag{6}$$

where K_s is the thermal conductivity of the solid (matrix) and n is a parameter dependent on the pore geometry (n = 1.5 for spherical pores).

Considering that ε = 0.59 (value of the pore volume fraction for a guest-free foam) and that the thermal conductivity of the Al-12 wt% Si alloy (K_s) was measured to be 179 $Wm^{-1}°C^{-1}$, the value estimated by Eq. (6) is 47 $Wm^{-1}°C^{-1}$ when n is assumed to be 1.5, which is in perfect agreement with the measured value, considering the experimental measurement error.

3.6. Pressure drop and permeability

The pressure drop across the Guefoam and packed bed was determined using the setup described in Fig. 1. Fig. 7a shows the resulting pressure drop curves.

As expected, the pressure drop caused by the packed bed of active phase particles is substantially higher than the pressure drop generated by the Guefoam. Unlike other foam materials, Guefoams can experience different pressure drops depending on the orientation (Fig. 7a). This is because guest phases can block the interconnecting windows and force the fluid to take less direct paths, resulting in higher pressure drops (Fig. 7b). The pressure drop of the Guefoam was measured in the horizontal orientation and in the vertical position with gas flow from top to bottom and

from bottom to top. Fig. 7a confirms, as expected in view of Fig. 7b, that the lowest pressure drop is achieved in the horizontal configuration. In this horizontal arrangement, gravity acts perpendicular to the fluid passage so that the guest phase particles lean on the lower cavity walls, away from the most direct path defined by the fluid as it passes through the material, thus offering less resistance to the fluid passage. In contrast, gravity and fluid passage are parallel in vertical arrangements and the guest phase particles lean on fluid-trajectory aligned cavity regions, sometimes even blocking the interconnecting windows that define the easiest fluid path and offering greater resistance to fluid passage.

The permeability values (k) can be obtained from the curves in Fig. 7a by quadratic fits according to Eq. (1). The results are summarized in Table 2, which shows that the Guefoam catalyst is 1.7–2.7 times more permeable than the packed bed.

3.7. Comparison of the catalytic performance of Guefoam and particle bed

The design of catalytic materials in heterogeneous catalysis is a complex process that must be considered from a holistic perspective. The success of a catalytic material in industry is not constrained to its catalytic activity, but encompasses other considerations, such as its pressure drop, which represents a large portion of the energy required to function as a catalyst, or its thermal conductivity, which allows for considerations of its scalability to useful dimensions. In this work, these considerations have been further explored in order to show a performance comparison between the studied systems, i.e. Guefoam and particle bed.

In [50], conversion efficiency and pressure drop were related in a parameter defined as catalytic performance index (I_p) to compare different reactors using the following equation (slightly rewritten to replace ΔP with $\Delta P/\Delta L$ to normalize the pressure drop with sample length):

$$I_p = \frac{-\ln(1 - \eta)}{\Delta P/\Delta L} \tag{7}$$

being η the conversion efficiency.

Fig. 8a shows the I_p values obtained from the experimental characterization as a function of the conversion temperature. The graph reveals that the Guefoam (washed and calcined) has the best performance as a catalytic reactor at temperatures above 350 °C, since the conversion efficiency/pressure drop ratio results in the highest I_p index.

The thermal conductivity and permeability of a catalytic material affect the heat transfer into or from the material, thus influencing the temperature gradients, which can ultimately have a significant impact on the catalytic performance of materials with large dimensions. In order to analyse the temperature gradients inside the Guefoam catalyst and the packed bed, a CFD modelling of the temperature profiles was performed. Fig. 8b and c shows radial temperature profiles on three y-z planes at 1, 15 and 29 cm inlet length of the Guefoam and the particulate bed (the dimensions and fluxes taken, which were explained in Section 2.7, correspond to those of a possible industrial application for the methanation reaction considered).

Significant differences are observed in the temperature gradients of the two systems considered. As expected, the temperature for both catalyst beds is higher near the outer walls than in the middle of the reactor, since the model assumes that heating is provided by an external heat source. The lowest temperature gradients were obtained for the Guefoam catalyst due to its metallic nature (Fig. 8b), while the highest gradients were obtained for the packed bed of active phase particles (Fig. 8c), which consists
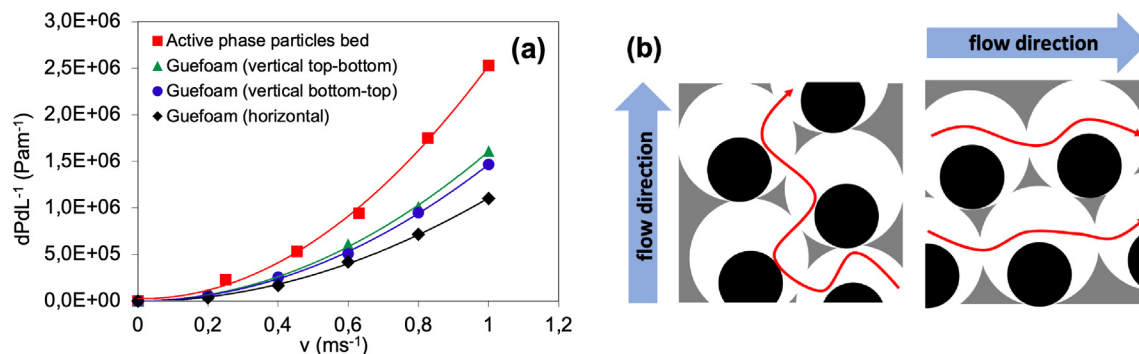
Table 2
Pore volume fraction (ε), thermal conductivity (K) and permeability (k) of the different materials herein characterized.

Material	ε	K ($Wm^{-1}°C^{-1}$)	k (m^2)
Guefoam catalyst (vertical; top–bottom flow)	0.35	43	1.49×10^{-9}
Guefoam catalyst (vertical; bottom-top flow)			1.06×10^{-9}
Guefoam catalyst (horizontal)			9.43×10^{-10}
Active phase particles bed	0.43	1.7	5.51×10^{-10}

Fig. 7. (a) Experimental results and second-degree polynomial fits of the pressure drop as a function of superficial velocity for the following materials: Guefoam in vertical configuration from top to bottom ($y = 1.59 \times 10^6 x^2 + 1.91 \times 10^4 x$; $R^2 = 0.999$), Guefoam in vertical configuration from bottom to top ($y = 1.45 \times 10^6 x^2 + 1.69 \times 10^4 x$; $R^2 = 0.999$), Guefoam in horizontal configuration ($y = 1.09 \times 10^6 x^2 + 1.21 \times 10^4 x$; $R^2 = 0.999$) and active phase particle bed ($y = 2.49 \times 10^6 x^2 + 3.27 \times 10^4 x$; $R^2 = 0.998$); (b) Illustrative diagram of vertical and horizontal configurations of pressure drop measurement in Guefoam.
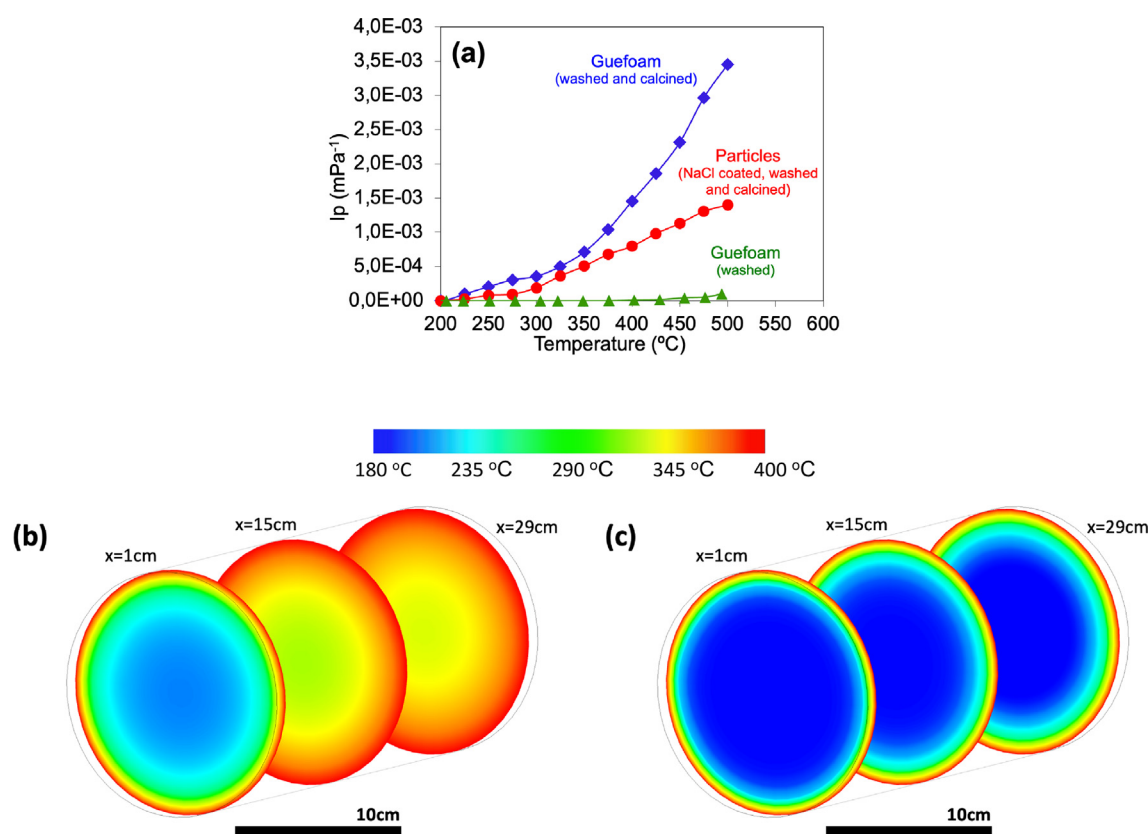

Fig. 8. (a) Catalytic performance index (I_p) as a function of conversion temperature; radial temperature profiles for the Guefoam (b) and active phase particle bed (c).

of metal oxides (mainly alumina and ceria) with poor thermal conductivity.

Thus, the temperature at the centre of the y-z plane, located 15 cm from the inlet, is 250 °C for the Guefoam catalyst, while it is significantly lower for the packed bed. Considering, for instance, that the onset temperature for CO_2 methanation is about 250 °C (see Fig. 5), the effective heating of the Guefoam catalyst allows a larger volume of the catalyst bed to have temperatures above the threshold required for the reaction.

4. Conclusions

The preparation and use of Guefoams as heterogeneous catalysts were investigated in this study. The general structure of the prepared Guefoam catalyst consists of an interconnected (or open-pore) Al-Si foam hosting freely moving guest phases in their cavities, since there is no chemical or physical matrix-guest bond. Alumina particles loaded with the Ni/CeO$_2$ active phase were used as the guest phase. A eutectic Al-12Si alloy was chosen for the foam body to lower the melting temperature and prevent thermal sintering of the active phase during liquid metal infiltration.

CO_2 methanation experiments were performed using the novel Guefoam catalyst as a reaction test. The obtained activity and CH_4 selectivity (close to 100%) were similar to the values obtained with a packed bed of the same active phase particles, but with the benefits of a structured reactor. Guefoam manufacture requires the coating of the active phase particles with a NaCl shell. The salt is dissolved once the Al-Si alloy is infiltrated to obtain the foam. As

L.P. Maiorano, C.Y. Chaparro-Garnica, E. Bailón García et al.

Materials & Design 217 (2022) 110619

shown by XPS characterization, the presence of chlorine anions poisons the active phase and inhibits the catalytic activity. A critical step in the Guefoam synthesis is the final calcination (500 °C; 4 h) to replace the chlorine with oxide anions, which only then ensure the catalytic activity.

The thermal conductivity of the Guefoam catalyst is significantly improved with regard to the packed bed of active phase particles. This reduces the temperature gradients in the catalytic reactor, as demonstrated by computational fluid dynamic modelling.

Pressure drop measurements showed that the permeability of the Guefoam catalyst is up to 2.7 times higher than that of the packed bed, resulting in a better catalytic performance index (I_p), especially at temperatures above 350 °C.

Beyond the specific conclusions drawn in the present study and to comment on the future perspectives that can be achieved with Guefoams, the authors foresee a great potential of these materials in the context of new challenges in heterogeneous catalysis, such as the design of multi-catalytic reactors or for tandem reactions by combining different guest phases as differentiated catalytic centres. The versatility in varying the GL and GO parameters in the different cavities of a material is a tool with enormous potential for the design of future catalytic reactors adapted to specific working conditions and in which the catalytic performance can be optimised to values adapted to particular needs.

Declaration of Competing Interest

The authors declare that they have no known competing financial interests or personal relationships that could have appeared to influence the work reported in this paper.

Acknowledgements

Data availability

The raw data required to reproduce these findings are available to download from [https://zenodo.org/deposit/5719300]. The processed data required to reproduce these findings are available to download from [https://zenodo.org/deposit/5719300].

Appendix A. Supplementary material

Supplementary data to this article can be found online at https://doi.org/10.1016/j.matdes.2022.110619.

References

[1] J.M. Molina-Jorda, Spanish Patent P201730890, 2017.
[2] J.M. Molina-Jorda, PCT Patent PCT/ES2018/070474, 2018.
[3] J.M. Molina-Jordá, Highly adsorptive and magneto-inductive Guefoams (multifunctional guest-containing foams) for enhanced energy- efficient preconcentration and management of VOCs, Appl. Mater. Interfaces 12 (2020) 11702–11712, https://doi.org/10.1021/acsami.9b22858.
[4] J.M. Molina-Jordá, Magneto-inductive open-cell cellular carbon composites with activated carbon as guest phase: Guefoams for energy-efficient VOCs management, Ceram. Int. 2022 (in press). doi:10.1016/j.ceramint.2022.03.008.
[5] A.J. Otaru, Review on processing and fluid transport in porous metals with focus on bottleneck structures, Met. Mater. Int. 26 (2020) 510–525, https://doi.org/10.1007/s12540-019-00345-9.
[6] T. Wan, Y. Liu, C. Zhou, X. Chen, Y. Li, Fabrication, properties, and applications of open-cell aluminum foams: A review, J. Mater. Sci. Technol. 62 (2021) 11–24, https://doi.org/10.1016/j.jmst.2020.05.039.
[7] A. Gancarczyk, K. Sindera, M. Iwaniszyn, M. Piatek, W. Macek, P.J. Jodlowski, et al., Metal foams as novel catalyst support in environmental processes, Catalysts 9 (2019) 587, https://doi.org/10.3390/catal9070587.
[8] S. Cimino, E.M. Cepollaro, L. Lisi, S. Fasolin, M. Musiani, L. Vázquez-Gómez, Ru/Ce/Ni metal foams as structured catalysts for the methanation of CO2, Catalysts 11 (2021) 13, https://doi.org/10.3390/catal11010013.
[9] H. Ma, K. Ma, J. Ji, S. Tang, C. Liu, W. Jiang, et al., Graphene intercalated Ni-SiO2/GO-Ni foam catalyst with enhanced reactivity and heat transfer con CO2 methanation, Chem. Eng. Sci. 194 (2019) 10–21, https://doi.org/10.1016/j.ces.2018.05.019.
[10] S. Li, G. Zhang, H. Zheng, Y. Zheng, P. Wang, Application of BiFeO3-based on nickel foam composites with a highly efficient catalytic activity and easily recyclable in Fenton-like process under microwave irradiation, J. Power Sources 386 (2018) 21–27, https://doi.org/10.1016/j.jpowsour.2018.03.027.
[11] L. Zhu, X. Guo, Y. Liu, Z. Chen, W. Zhang, K. Yin, et al., High-performance Cu nanoparticles/three-dimensional graphene/Ni foam hybrid for catalytic and sensing applications, Nanotechnology 29 (2018), https://doi.org/10.1088/1361-6528/aaaac6.
[12] H.B. Dai, Y. Liang, P. Wang, X.D. Yao, T. Rufford, M. Lu, et al., High-performance cobalt–tungsten–boron catalyst supported on Ni foam for hydrogen generation from alkaline sodium borohydride solution, 33 (2008) 4405–4412. doi:10.1016/j.ijhydene.2008.05.080.
[13] H. Liu, S. Li, S. Zhang, J. Wang, G. Zhou, L. Chen, et al. Catalytic performance of novel Ni catalysts supported on SiC monolithic foam in carbon dioxide reforming of methane to synthesis gas, 9 (2008) 51–54. doi:10.1016/j.catcom.2007.05.002.
[14] N. Zhou, S. Liu, Y. Zhang, L. Fan, Y. Cheng, Y. Wang, et al., Silicon carbide foam supported ZSM-5 composite catalyst for microwave-assisted pyrolysis of biomass, Bioresour. Technol. 267 (2018) 257–264, https://doi.org/10.1016/j.biortech.2018.07.007.
[15] U. Betke, S. Proemmel, J.G. Eggebrecht, S. Rannabauer, A. Lieb, M. Scheffler, et al., Micro-Macroporous Composite Materials: SiC Ceramic Foams Functionalized with the Metal Organic Framework HKUST-1, Chem.-Ing.-Tech. 88 (2016) 264–273, https://doi.org/10.1002/cite.201500141.
[16] J.M. Molina-Jordá, Mesophase pitch-derived graphite foams with selective distribution of TiC nanoparticles for catalytic applications, Carbon 103 (2016). doi:10.1016/j.carbon.2016.02.051.
[17] I.V. Yentekakis, F. Dong, Grand Challenges for Catalytic Remediation in Environmental and Energy Applications Toward a Cleaner and Sustainable Future, Front. Environ. Chem. 1 (2020) 1–14, https://doi.org/10.3389/fenvc.2020.00005.
[18] H. Wang, B. Yuan, R. Hao, Y. Zhao, X. Wang, A critical review on the method of simultaneous removal of multi-air-pollutant in flue gas, Chem. Eng. J. 378 (2019), https://doi.org/10.1016/j.cej.2019.122155.
[19] Y.A.M. Esa, N. Sapawwe, A short review on carbon dioxide (CO2) methanation process, Mater. Today:. Proc. 31 (2020) 394–397, https://doi.org/10.1016/j.matpr.2020.07.191.
[20] C. Italiano, J. Llorca, L. Pino, M. Ferraro, V. Antonucci, A. Vita, CO and CO2 methanation over Ni catalysts supported on CeO2, Al2O3 and Y2O3 oxides, Appl. Catal. B: Environ. 264 (2020), https://doi.org/10.1016/j.apcatb.2019.118494.
[21] U. Ulmer, T. Dingle, P.N. Duchesne, R.R.H. Morris, A. Tavasoli, T. Wood, et al., Fundamentals and applications of photocatalytic CO2 methanation, Nat. Commun. 10 (2019) 3169, https://doi.org/10.1038/s41467-019-10996-2.
[22] J. Ashok, S. Pati, P. Hongmanorom, Z. Tianxi, C. Junmei, S. Kawi, A review of recent catalyst advances in CO2 methanation process, Catal. Today 356 (2020) 471–489, https://doi.org/10.1016/j.cattod.2020.07.023.
[23] J.C. Matsubu, V.N. Yang, P. Christopher, Isolated metal active site concentration and stability control catalytic CO2 reduction selectivity, J. Am. Chem. Soc. 137 (2015) 3076–3084, https://doi.org/10.1021/ja5128133.
[24] F. Wang, S. He, H. Chen, B. Wang, L. Zheng, M. Wei, et al., Active Site Dependent Reaction Mechanism over Ru/CeO2 Catalyst toward CO2 Methanation, J. Am. Chem. Soc. 138 (2016) 6298–6305, https://doi.org/10.1021/jacs.6b02762.
[25] K. Ray, G. Deo, A potential descriptor for the CO2 hydrogenation to CH4 over Al2O3 supported Ni and Ni-based alloy catalysts, Appl. Catal. B: Environ. 218 (2017) 525–537, https://doi.org/10.1016/j.apcatb.2017.07.009.
[26] V. Alcalde-Santiago, A. Davó-Quiñonero, D. Lozano-Castelló, A. Quindimil, U. De-La-Torre, B. Pereda-Ayo, et al., Ni/LnOx Catalysts (Ln=La, Ce or Pr) for CO2 Methanation, ChemCatChem 11 (2019) 810–819. doi:10.1002/cctc.201801585.
[27] N. Rui, X. Zhang, F. Zhang, Z. Liu, X. Cao, Z. Xie, et al., Highly active Ni/CeO2 catalyst for CO2 methanation: Preparation and characterization, Appl. Catal. B: Environ. 282 (2021), https://doi.org/10.1016/j.apcatb.2020.119581.

L.P. Maiorano, C.Y. Chaparro-Garnica, E. Bailón García et al.

Materials & Design 217 (2022) 110619

[28] L. Shen, J. Xu, M. Zhu, Y. Han, Essential role of support for nickel-based CO2 methanation catalysts, Catalysis 10 (2020) 14581–14591, https://doi.org/10.1021/acscatal.0c03471.

[29] S. Tada, H. Nagase, N. Fujiwara, R. Kikuchi, What are the best active sites for CO2 methanation over Ni/CeO2?, Energy Fuels 35 (2021) 5241–5251, https://doiorg/10.1021/acs.energyfuels.0c04238.

[30] H.A. Kuchek, United States Patent 3236706, 1964.

[31] N.G. Carlson, United States Patent 3210166, 1967.

[32] J. Molina, R. Saravanan, R. Arpón, C. García-Cordovilla, E. Louis, Pressure infiltration of liquid aluminium into packed SiC particulate with a bimodal size distribution, Acta Materialia 50 (2002) 247–257.

[33] N. Altinkok, A. Demir, I. Ozsert, Processing of Al2O3/SiC ceramic cake preforms and their liquid Al metal infiltration, Compos. A Appl. Sci. Manuf. 34 (2003) 577–582, https://doi.org/10.1016/S1359-835X(03)00125-8.

[34] C. Garcia-Cordovilla, E. Louis, J. Narciso, Pressure infiltration of packed ceramic particulates by liquid metals, Acta Mater. 47 (1999) 4461–4479, https://doi.org/10.1016/S1359-6454(99)00318-3.

[35] L.P. Maiorano, J.M. Molina, Challenging thermal management by incorporation of graphite into aluminium foams, Mater. Des. 158 (2018) 160–171, https://doi.org/10.1016/j.matdes.2018.08.026.

[36] L.P. Maiorano Lauría, J.M. Molina Jordá, Open-pore foams modified by incorporation of new phases: Multiphase foams for thermal, catalytic and medical emerging applications, Foams – Emerg. Technol. (2019) 1–21, https://doi.org/10.5772/intechopen.88977.

[37] L.P. Maiorano, J.M. Molina, Guiding heat in active thermal management: One-pot incorporation of interfacial nano-engineered aluminium/diamond composites into aluminium foams, Compos. A Appl. Sci. Manuf. 133 (2020), https://doi.org/10.1016/j.compositesa.2020.105859.

[38] P.T. Garrity, J.F. Klausner, R. Mei, Performance of aluminum and carbon foams for air side heat transfer augmentation, J. Heat Transfer 132 (2010) 1–9, https://doi.org/10.1115/1.4002172.

[39] Y. Li, L. Gong, B. Ding, M. Xu, Y. Joshi, Thermal management of powder electronics with liquid cooled metal foams heat sink, Int. J. Therm. Sci. 163 (2021), https://doi.org/10.1016/j.ijthermalsci.2020.106796.

[40] M.P. Lai, W.H. Laia, R.F. Horng, C.Y. Chen, W.C. Chiu, S.S. Su, et al., Experimental study on the performance of oxidative dry reforming from simulated biogas, Energy Procedia 29 (2012) 225–233, https://doi.org/10.1016/j.egypro.2012.09.028.

[41] Y.S. Mok, E. Jwa, H.W. Lee, Production of methane from carbon monoxide and carbon dioxide in a plasma-catalytic combined reactor system, Int. J. Sustain. Dev. Plann. 8 (2013) 186–196, https://doi.org/10.2495/SDP-V8-N2-186-196.

[42] C.V. Miguel, M.A. Soria, A. Mendes, L.M. Madeira, Direct CO2 hydrogenation to methane or methanol from post-combustion exhaust streams - A thermodynamic study, J. Nat. Gas Sci. Eng. 22 (2015) 1–8, https://doi.org/10.1016/j.jngse.2014.11.010.

[43] F. Lin, Q. Wang, X. Huang, J. Jing, Investigation of chlorine-poisoning mechanism of MnOx/TiO2 and MnOx-CeO2/TiO2 catalysts during o-DCBz catalytic decomposition: Experiment and first-principles calculation, J. Environ. Manage. 298 (2021), https://doi.org/10.1016/j.jenvman.2021.113454.

[44] M. Li, F. Bi, Y. Xu, P. Hao, K. Xiang, Y. Zhang, et al., Effect of residual chlorine on the catalytic performance of Co3O4 for CO oxidation, ACS Catal. 9 (2019) 11676–11684, https://doi.org/10.1021/acscatal.9b03797.

[45] R. Cucciniello, A. Intiso, T. Siciliano, A.E. Palomares, J. Martínez-Triguero, J.L. Cerrillo, et al., Oxidative degradation of trichloroethylene over Fe2O3-doped Mayenite: chlorine poisoning mitigation and improved catalytic performance, Catalysts 9 (747) (2019) 2–13, https://doi.org/10.3390/catal9090747.

[46] A. Caballero, J.P. Holgado, V.M. Gonzalez-Delacruz, S.E. Habas, T. Herranz, M. Salmeron, In situ spectroscopic detection of SMSI effect in a Ni/CeO2 system: Hydrogen-induced burial and dig out of metallic nickel, Chem. Commun. 46 (2010) 1097–1099, https://doi.org/10.1039/b920803h.

[47] H. Li, H. Li, W.L. Dai, W. Wang, Z. Fang, J.F. Deng, XPS studies on surface electronic characteristics of Ni-B and Ni-P amorphous alloy and its correlation to their catalytic properties, Appl. Surf. Sci. 152 (1999) 25–34, https://doi.org/10.1016/S0169-4332(99)00294-9.

[48] Z. Hou, O. Yokota, T. Tanaka, T. Yashima, Characterization of Ca-promoted Ni/α-Al2O3 catalyst for CH4 reforming with CO2, Appl. Catal. A: General 253 (2003) 381–387, https://doi.org/10.1016/S0926-860X(03)00543-X.

[49] E. Heracleous, A.F. Lee, K. Wilson, A.A. Lemonidou, Investigation of Ni-based alumina-supported catalysts for the oxidative dehydrogenation of ethane to ethylene: Structural characterization and reactivity studies, J. Catal. 231 (2005) 159–171, https://doi.org/10.1016/j.jcat.2005.01.015.

[50] T. Lucci, A.D. Torre, G. Montenegro, P.D. Eggenschwiler, On the catalytic performance of open cell structures versus honeycombs, Chem. Eng. J. 264 (2014) 514–521. doi:10.1016/ j.cej.2014.11.080.